JOURNAL OF AIRCRAFT
Vol. 40, No. 3, May–June 2003

Aerooptical Design of a Long-Range Oblique Photography Pod

Yuval Levy*
Technion—Israel Institute of Technology, 32000 Haifa, Israel
Mark Hornstein†
ELOP Electrooptics Industries, Ltd., 76111 Rehovot, Israel
and
David A. Lednicer‡
Analytical Methods, Inc., Redmond, Washington 98052

In recent years, the long-range oblique photography (LOROP) technique has become a preferred technique for aerial photography. The LOROP technique provides a safer mission flight profile for medium- and high-altitude photography. Most of the LOROP cameras are designed for pod applications and not for internal aircraft installation. The technique requires that the optical windows would reside on flat planes on the sides of the containing pod. Consequently, performance of the LOROP camera strongly depends on the quality of the flow around the windows. Furthermore, issues of aerooptical qualities of the flow must be taken into account in the design of the pod geometry. The aerooptical design process of the LOROP pod is described. The design was conducted using computational fluid dynamics methods. Results from wind-tunnel experiments and a photograph taken by the camera during a supersonic flight are presented to validate the numerical simulations results.

Introduction

THE need to collect intelligence through high-resolution photography with high-safety-profile missions will continue to increase in the years ahead. There are four main types of reconnaissance missions, namely, penetrating overflight, penetrating side oblique depression angle (SODA), long-range oblique photography (LOROP), and satellite missions (Fig. 1). All of the types, except the satellite-type mission, require that the camera be mounted on an aircraft.

In the penetrating-type mission, an aircraft carrying the camera is flown above the photographed area at a relatively low altitude, whereas in the penetrating SODA type, the camera is used to photograph the area that is located to the side of the aircraft at a moderate angle, still at a low-to-medium altitude flight. Both of these mission types require that the aircraft be flown close to the photographed area, and therefore, the pilot of the aircraft is placed at risk.

The LOROP-type mission photographs areas that are located to the side of the aircraft at a large angle such that areas at distances in excess of 50 km can be photographed, thus, providing the means for secured standoff flights. An example of a LOROP camera in a pod mounted configuration is the Raptor pod, which consists of the Raytheon Optical System, Inc., DB-110 sensor.[1] No details were given as to the aerooptical performance of the camera.

The large photography angle requires care in the design of the pod carrying the camera. The performance of a camera may be greatly affected by an improper design, which in turn will affect the flow surrounding the pod. Special care must be taken in the design of the pod, especially for the transonic and supersonic flow regimes, and therefore, aerooptical considerations are added to the aerodynamic considerations.

The LOROP system described herein is installed in a standard fuel tank configuration with two flat optical windows (Fig. 2). A forward scoop and two rear inlets were added for the air conditioning systems. The design process of the pod included numerical simulations of the flow about the pod to assure a smooth and shock free flow in the vicinity of the windows. It is the purpose of this paper to describe in detail the aerooptical design process, the numerical simulations, and wind-tunnel test results that confirm the aerooptical performance of the pod.

Aerooptical Phenomena and Optical Degradation

A camera residing in a high-speed aircraft is susceptible to a degradation of its photographic quality due to compressibility effects induced by the surrounding flowfield. The optical loses are due to changes in the index of refraction, which are caused by density fluctuations. The index of refraction fluctuations n' is related to the density fluctuations ρ' by the Gladstone–Dale relation

$$n' = G\rho' \tag{1}$$

where G is the Gladstone–Dale constant (see Ref. 2). For the standard atmosphere, the Gladstone–Dale constant is $G = 0.226 \times 10^{-3}$ m^3/kg.

The first aerooptical source of optical degradation is turbulence in the boundary and shear layers. Three principal optical distortions may be caused by turbulence. Small-scale turbulence causes a loss of beam contrast, intermediate-scale turbulence causes beam spread and, therefore, causes image blurring, and large-scale turbulence causes beam jitter.[2] The boundary layers of high-speed aircraft are fully turbulent and thin and, therefore, usually present a short optical path. However, if separation occurs, they can present a long optical path and can be the source of severe optical degradation. The wavefront error due to turbulence can be estimated by[2,3]

$$\sigma^2 = 2G^2 \int_0^L \bar{\rho}'^2(z)\Lambda(z)\,\mathrm{d}z \tag{2}$$

where σ is the root mean square wave front error in micrometers, L is the path through the turbulent region, and Λ is the Eulerian integral scale. Assume that the boundary layer remains attached; then the two most important factors affecting the wave front error are the density fluctuations and the boundary-layer thickness. Typical density fluctuations at transonic Mach numbers are of the order of 1–2% of the local mean density.

Density changes due to shocks present the second source of optical degradation. Shocks occur whenever the local flow velocity

Received 5 October 2001; revision received 12 November 2002; accepted for publication 2 December 2002.

*Senior Lecturer, Faculty of Aerospace Engineering. Senior Member AIAA.
†Project Manager, Airborne Reconnaissance Systems Business Unit.
‡Deputy Director, Aerospace Applications. Senior Member AIAA.

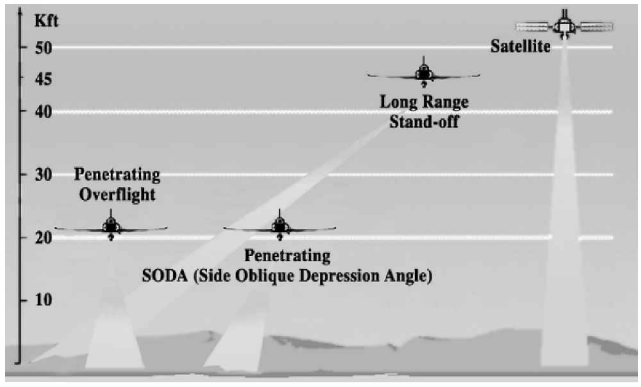

Fig. 1 Typical reconnaissance missions.

Fig. 2 LOROP pod (photograph courtesy of ELOP Electrooptic Industries, Inc.).

around obstacles exceed Mach 1. There are also "recovery shocks" in transonic flows even with the absence of any obstacles. Because of the large density changes across shocks, they cause a large variation to the index of refraction along an optical beam path. In addition, flow unsteadiness that is common in transonic flow causes the shock location to vary in time. Therefore, density changes associated with shocks present the most important source for aerooptical degradation.

The last source for optical degradation is density changes due to the airflow about the aircraft, its neighboring stores and pylons, and various obstacles. These density changes are significantly smaller than density changes caused by shocks but can present a long optical path.

These three sources for aero-optical degradation dictated the design process. Because transition to turbulence can not be prevented by conventional means, most of the efforts were directed at eliminating shocks and flow separation from the windows area. In addition, it was verified that the effects of near-field density changes due to the aircraft and its external stores were negligible.

Original Pod Geometry in Supersonic Flow

The original pod geometry, constrained by the similarity to the fuel tank and the need to have a flat surface for the optical window, had a cavity to accommodate the window. Numerical simulations of the flow around the pod in freestream were conducted using a full Navier–Stokes code (see Refs. 4–6). The use of the full Navier–Stokes equations provided the means to examine flow separation and shock-induced separation phenomena.

The computational mesh consisted of 43 equispaced circumferential planes extending around half of the body, and a symmetry boundary condition was employed at the symmetry plane. The symmetry assumption is valid as long as the simulations are conducted at low angles of attack. In each circumferential plane, the mesh contained 50 radial points between the body surface and the computational outer boundary and 129 axial points between the nose and the rear of the body. No-slip, adiabatic wall boundary conditions were employed at the body surface, and zero-order extrapolation was employed at the rear of the body.

In all of the Navier–Stokes simulations conducted here, the flow was assumed to be fully turbulent. The transonic and supersonic Mach numbers considered imply that transition to turbulence occurs within the first few centimeters of the pod. The Baldwin–Lomax turbulence model[7] with the Degani–Schiff[8–10] modification was utilized to model the turbulence.

The pod was designed to operate in high subsonic, transonic, and supersonic flow conditions, and therefore, a numerical simulation at a Mach number of $M_\infty = 1.2$ and an angle of attack of $\alpha = 1.0$ deg was conducted. Figure 3 shows the shock structure of the flow about the pod. The shocks are described by shaded triangles that are normal to the shock surface. The bow shock surrounding the nose of the pod is accompanied by an oblique shock generated by the forward-facing step of the cavity. Because the optical path of a beam intersects the bow shock at a large angle, the shock-induced beam deflection is not expected to be a source of optical degradation. However, the oblique shock is located in the middle of the window area and, therefore, should cause large density variations.

Figure 4 shows contours of the density distribution along a cut across the optical window. The density distribution confirms the location of the oblique shock in Fig. 3. The sharp density gradients

Fig. 3 Fuel tank with a cavity at Mach number $M_\infty = 1.2$, shocks structure.

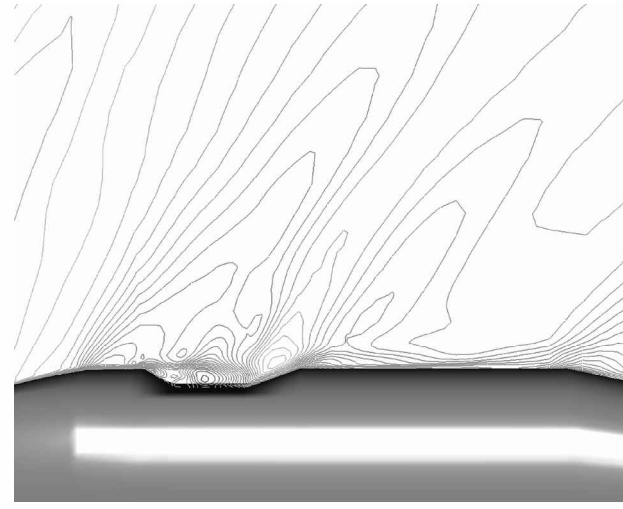

Fig. 4 Fuel tank with a cavity at Mach number $M_\infty = 1.2$, density distribution.

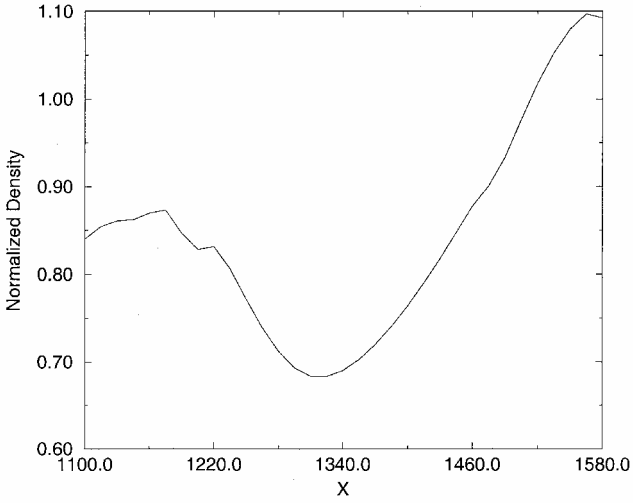

Fig. 5 Normalized density variation at the edge of the cavity.

Fig. 6 Original pod at Mach number $M_\infty = 1.2$, skin-friction lines shaded by values of local pressure.

around the cavity area are caused by the shock. Such density gradients would result in large changes to the index of refraction, which in turn would cause a blur of the image. The effect of the oblique shock is so severe because it resides within the window area. The density variations cause a significant change to the index of refraction, which in turn sharply changes the optical path of adjacent beams. Figure 5 shows normalized density variations (with respect to freestream density) along the edge of the cavity. The X coordinate is measured from the nose of the pod (in millimeters). The density jump across the oblique shock is approximately 40% and so is the index of refraction jump. This is due to the linear relation between density variations and index of refraction variations [Gladstone–Dale relation, Eq. (1)].

In addition to density variations around the window, Fig. 4 shows that the flow in the cavity is fully separated. A separation bubble is clearly seen right above the center of the window. As already mentioned, the turbulent separated bubble would cause serious optical degradation. To further illustrate the separation effect on the surface of the window, skin-friction lines on the body are presented in Fig. 6 using shaded texture.[11–14] The texture representation is created by smearing noise along the vector field in question. In this case, the wall shear vector is represented by the velocity vector at the first shell of points above the body surface. When using color, the texture may be color coded by the pressure such that "hot" colors (magenta and red) represent high pressure, whereas "cold" colors (blue and cyan) represent low pressure. Colored skin-friction lines simulate a combination of pressure sensitive paint and surface oil-flow representation of the flow. The various shades of gray in Fig. 6 illustrate the behavior of the pressure field and its gradient on the body surface. The topology of the lines in the cavity point to massive separation of the flow throughout the cavity. The separation is caused both by the backward- and forward-facing steps that compose the upstream and downstream edges of the cavity, respectively. The flow separation, in addition to the aforementioned oblique shock, would cause an uncorrectable blur to the image and would render the camera useless. Moreover, the flow around a cavity in supersonic flow conditions is known to be highly unsteady.[15–17] Such unsteadiness would cause additional changes in air properties around the cavity and, therefore, would hinder the camera's performance even further.

Numerical Simulations of the Pod in Freestream

To avoid the problems caused by the oblique shock and the flow separation, the pod was modified. The fuel tank was cut along a plane tangent to the window surface. The cut in the front part of the plane was kept sharp to guarantee that the shock that is generated on the plane remains close to the cut and would not oscillate back and forth along the plane. The sharp cut is in contrast to the aerodynamics considerations because it would cause local flow separation. However, the sharp cut is necessary to "trap" the transonic shock far ahead of the window. A forward scoop and two rear inlets were added for the air conditioning systems. The rear inlets were extended to the side so that the geometry of the rear section coincides with that of the original fuel tank.

The numerical simulations of the flow around the pod in free-stream were conducted using the same full Navier–Stokes code. The computational mesh consisted of 121 equispaced circumferential planes extending around the complete body, that is, no symmetry is assumed, and a periodic boundary condition was implemented. In each circumferential plane, the mesh contained 60 radial points between the body surface and the computational outer boundary and 77 axial points between the nose and the rear of the body. The rear inlets and forward scoop were smoothed to provide a better simulation of the flow, that is, to provide a smaller blockage of the flow.

Flow at Mach Number $M_\infty = 1.2$

Figure 7 shows the density distribution along the flat plane. As a result of the planar cut, density variations along the window region are negligible even though the flow is supersonic. The shock seen in Figs. 3 and 4 no longer exists. Density changes around the window area are limited to 2–3%, of the order of density variations that would be caused by turbulence. The shock that is generated at the tip of the pod does not interfere with the flow in the window region. A second shock is apparent right before the rear inlet, but its effect is localized, and it does not affect the window region.

Flow at Mach Number $M_\infty = 0.9$

The pod is designed to operate in high subsonic and transonic flow conditions, and therefore, numerical simulations at a Mach

Fig. 7 Pod at Mach number $M_\infty = 1.2$, density distribution.

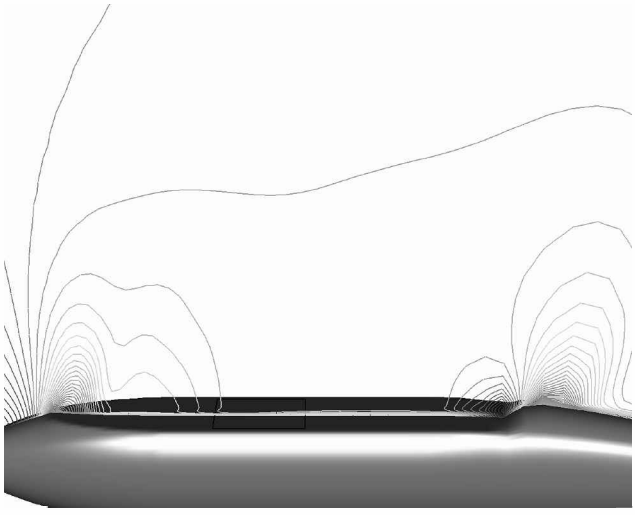

Fig. 8 Pod at Mach number $M_\infty = 0.9$, density distribution.

Fig. 9 Pod at Mach number $M_\infty = 0.9$, skin-friction lines shaded by values of local pressure.

number of $M_\infty = 0.9$ were conducted. Figure 8 shows the density distribution along the flat plane. Density variations along the window region are negligible. A shock is generated well ahead of the window due to the acceleration of the flow at the fore part of the flat plane. The sharp cut ensures that this shock remains well ahead of the window at all times, even at higher transonic speeds and even when unsteadiness is in play. Furthermore, numerical simulations conducted at a Mach number of $M_\infty = 0.95$ show that the shock remains well forward of the window.

Figure 9 shows the skin-friction lines on the body surface. The skin-friction lines around the window area are smooth, which shows that the flow is not separated. A close examination of the skin-friction lines shows that the shock-induced separation due to the transonic shock is localized to the shock area (right after the sharp cut) and that the flow around the window area is attached. The boundary-layer thickness around the window area is approximately 0.01 m, and therefore, the wave front error due to turbulence would cause only a small optical degradation.

Full Aircraft Simulations

Numerical simulations of the complete aircraft with stores were conducted using the Euler code MGAERO.[18] The full aircraft flow simulations were conducted to examine the effect of the aircraft, the pylon, and neighboring stores on the flow around the windows. Because the angle-of-attack range of a typical mission is low, no flow separation was expected to occur about the aircraft and the external stores. In addition, the flow about the modified pod was shown to be mostly attached. Thus, by choosing an Euler code, the flow can be satisfactorily and cheaply (in terms of computer resources) analyzed without the need to solve the viscous turbulent flow about the aircraft and its stores. The inflow through the rear inlets and forward scoop were estimated and used as input to the flow solver. The configuration of the aircraft included fuel tanks mounted in neighboring stations of the aircraft.

The flow conditions for the numerical simulations were chosen to cover the critical operational conditions of the pod, that is, transonic Mach numbers. Numerical simulations were conducted at Mach numbers of $M_\infty = 0.9$, 1.1, and 1.2 at appropriate flight heights. The flight height is used to determine the angle of attack that is required for straight and level flight for the corresponding flow conditions. For each simulation, the angle of attack was iterated until the aircraft trim was obtained, that is, the lift was equal to the aircraft weight with zero moments. Results from the numerical simulations at $M_\infty = 0.9$ were similar to those conducted for the pod in freestream. A normal shock was observed on the fore part of the flat plane, and the flow around the window area was smooth.

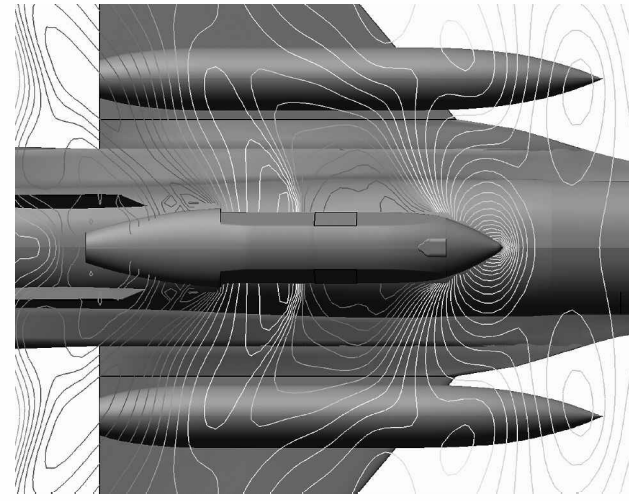

Fig. 10 Typical combat aircraft at Mach number $M_\infty = 1.1$, angle of attack $\alpha = 1.6$ deg, Mach contours.

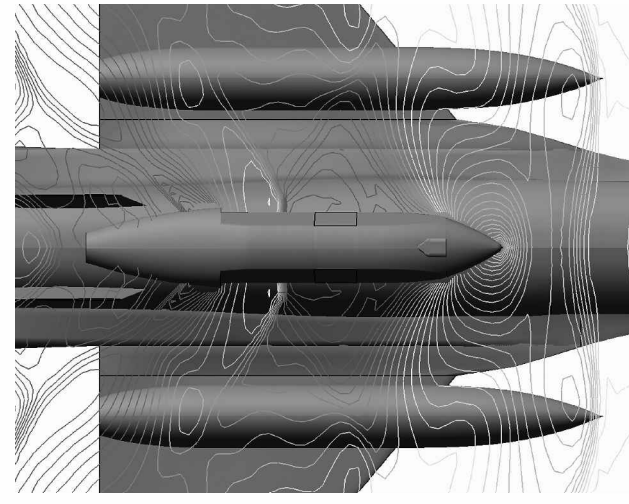

Fig. 11 Typical combat aircraft at Mach number $M_\infty = 1.2$, angle of attack $\alpha = 4.3$ deg, Mach contours.

Flow at Mach Number $M_\infty = 1.1$

The Mach number contours for the flow at $M_\infty = 1.1$ are presented in Fig. 10. At this transonic Mach number, a shock is generated on the pylon, behind the window area. The pressure jump as well as density jump are felt across the flat plane, behind the window, as shown by the Mach number changes. The Mach number contours also show that there is no interference from neighboring stores and that the interaction between the shocks upstream of the pod, caused by the presence of neighboring stores, does not have any effect on the flow around the window area.

Flow at Mach Number $M_\infty = 1.2$

The Mach number contours for the flow at $M_\infty = 1.2$ are presented in Fig. 11. At this Mach number, the shock generated by the pylon appears farther downstream, far from the window area. Similar to the case of $M_\infty = 1.1$, the Mach contours clearly show that neighboring stores do not affect the flow in the window area.

The simulations of the flows about the full aircraft show that the flow around the window area is shock free for all flow conditions that are of importance for aerooptical performance. At $M_\infty = 0.9$, there is a shock well ahead of the window; at $M_\infty = 1.1$, the pylon

shock is behind the window; and at $M_\infty = 1.2$, the pylon shock is well behind the window.

Wind-Tunnel Pressure Measurements

To verify the results obtained by computational means, wind-tunnel tests were conducted at the Israel Aircraft Industries, Inc., trisonic wind tunnel with a 15:1 aircraft model and an instrumented pod for pressure measurements. The aircraft configuration included fuel tanks in neighboring stations. There were 20 pressure taps located in the window area and 10 pressure taps located before and after the window. The angles of attack were chosen as typical angles for straight and level flight.

Pressure Measurements at Mach Number $M_\infty = 0.9$

The pressure measurements were utilized to create contours of pressure. Figure 12 shows measured pressure contours for the flow at an angle of $\alpha = 1.4$ deg. The flow is from left to right. Note that the pressure difference between consecutive contour lines is 0.02 psi. The small decline in the pressure seen in Fig. 12 may be the result of a slight side-slip angle of the whole model. The pressure variations are small and indicate that no shocks are present in the window area. These results are consistent with those of the numerical simulations. An additional run at a higher angle of attack of $\alpha = 3.4$ deg showed no significant differences in the pressure distribution, thus, indicating that the flow in the window area is smooth and stable and that the transonic shock on the flat plane is trapped well ahead of the window.

Pressure coefficients were calculated, and the results are shown in Fig. 13. The four lines represent four different heights along the window. The Z coordinate is measured from the bottom part of the window whereas the X coordinate is measured from the nose of the pod. The highest line (at $Z = 400$ mm) is the line closest to the pylon and the lowest line (at $Z = 30$ mm) is the one at the bottom part of the window. The highest and lowest lines are actually located on the window frame. The small decrease in the pressure coefficient is consistent with the pressure contours presented in Fig. 12. The results are also consistent with the results from the numerical simulations as presented in preceding sections.

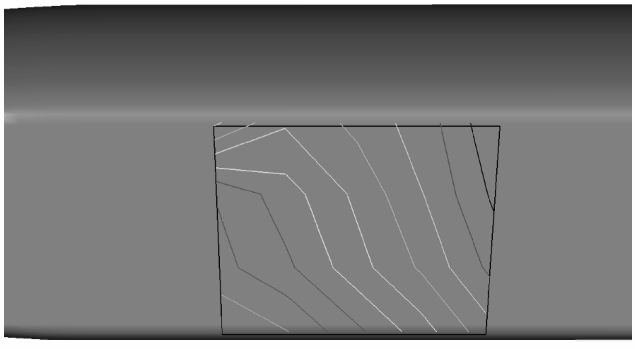

Fig. 12 Surface pressure contours, $M_\infty = 0.9$, angle of attack $\alpha = 1.4$ deg.

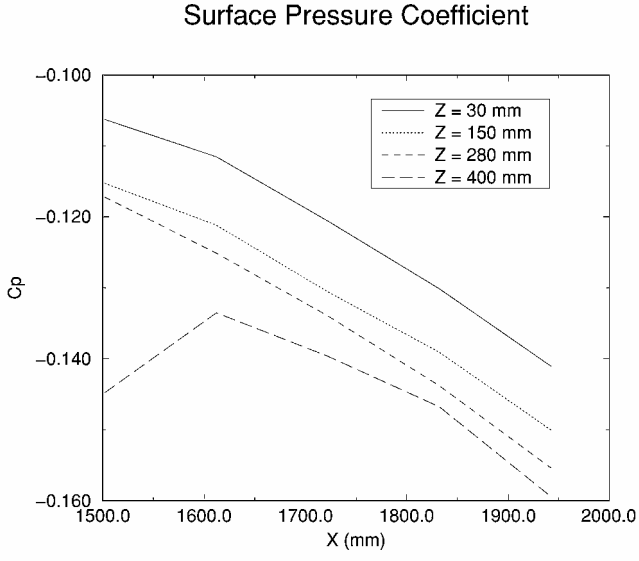

Fig. 13 Surface pressure coefficient, $M_\infty = 0.9$, angle of attack $\alpha = 1.4$ deg.

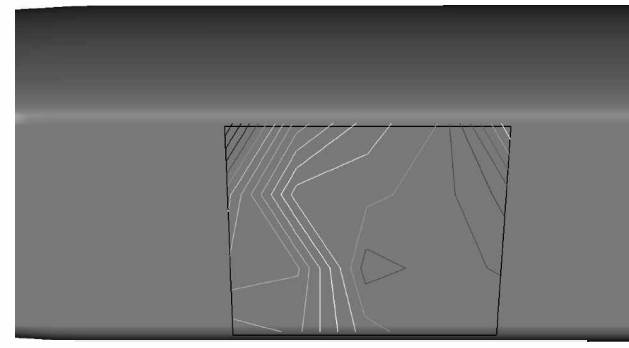

Fig. 14 Surface pressure contours, $M_\infty = 1.1$, angle of attack $\alpha = 1.4$ deg.

Pressure Measurements at Mach Number $M_\infty = 1.1$

Figure 14 shows pressure contours for the flow at an angle of $\alpha = 1.4$ deg. The pressure difference between consecutive contour lines in Fig. 14 is 0.2 psi. In contrast to the full aircraft numerical simulations, the shock that is caused by the pylon is located above the window area, upstream of the location predicted by the numerical simulations. The pressure contours show that the effect of the shock is largest along the top line and that the effect declines when moving toward the lower part of the window.

The reasons for the differences between the numerical simulations and the wind-tunnel results are numerous. One possible reason is that, in the experiment, the rear inlets were blocked and, therefore, presented a 100% blockage of the flow, compared to the real inlets as were simulated numerically. This might have caused the shock to move upstream. Another possible reason is the growth of the boundary layers.

As was already mentioned, the wind-tunnel model for all of the experiments was a 15:1 model. Such a model may realistically simulate most of the flow phenomena. However, certain phenomena, such as boundary-layer growth, are nonlinear and, therefore, wind-tunnel experimental results may differ from the full-scale aircraft results. Elementary analysis of boundary-layer growth, assuming flat plate behavior, shows that boundary-layer thickness on the model can be as large as 1.5 times the relative thickness of the boundary layer on the full-scale aircraft. This fact is especially significant when analyzing the flow at the gap between the fuselage, the pylon, and the pod. The larger boundary layer at the experiment causes a larger blockage of the flow and, therefore, the transonic shock at Mach number $M_\infty = 1.1$ moves forward in the wind-tunnel test.

The decreasing effect of the pylon shock is more evident from the pressure coefficient distribution along the window as presented in Fig. 15. The four lines correspond to the same heights as in Fig. 13. The biggest pressure rise is for the line at $Z = 400$ mm, and the pressure rise declines as Z decreases. This is consistent with the assumption that the shock is generated by the pylon. It also shows that the largest pressure gradients are at the top part of the window, whereas pressure gradients on the lower part of the window are significantly smaller.

To verify that the pressure jump is not caused by shocks generated on neighboring stores, an additional test was conducted. The configuration was identical except for the removal of the neighboring fuel tanks. Figure 16 shows the pressure coefficient distribution for this wind-tunnel run. The pressure jump is still apparent, and from the behavior of the pressure coefficient along different heights, it is clear that the pressure rise is caused by the pylon shock.

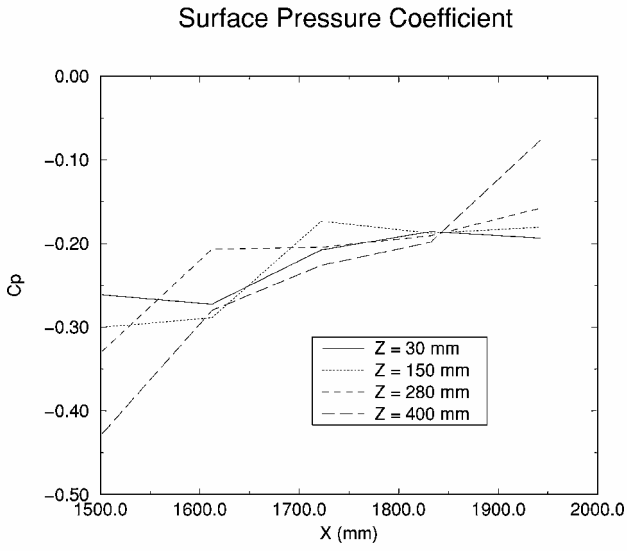

Fig. 15 Surface pressure coefficient, $M_\infty = 1.1$, angle of attack $\alpha = 1.4$ deg.

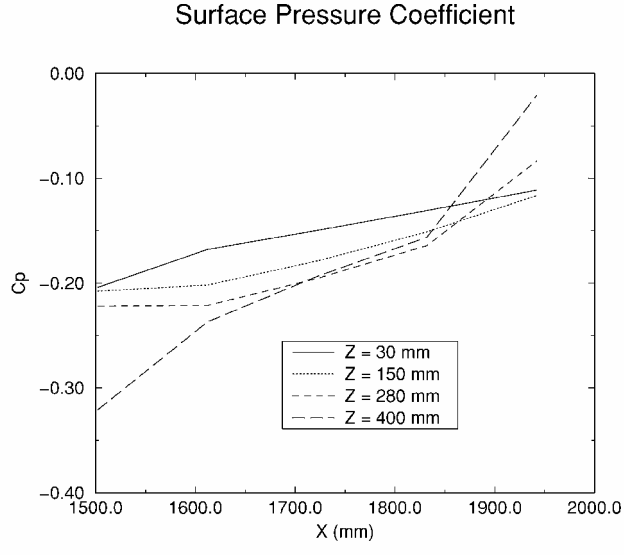

Fig. 16 Surface pressure coefficient, $M_\infty = 1.1$, angle of attack $\alpha = 1.4$ deg, without stores.

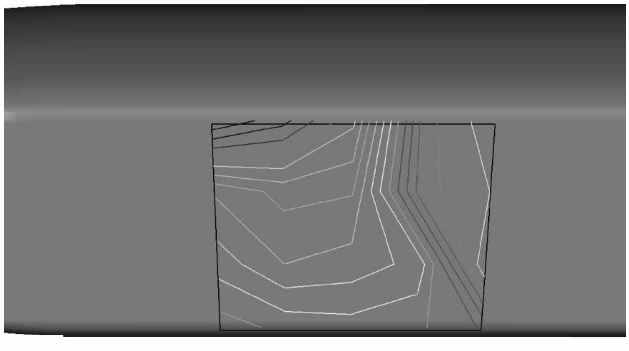

Fig. 17 Surface pressure contours, $M_\infty = 1.2$, angle of attack $\alpha = 1.4$ deg.

Pressure Measurements at Mach number $M_\infty = 1.2$

Figure 17 shows pressure contours for the flow at an angle of attack of $\alpha = 1.4$ deg. The pressure difference between contour lines in Fig. 17 is also 0.2 psi. A pressure rise around the top part of the window is present. However, it affects only a small portion in the rear upper part of the window. The pressure contours clearly show that the pressure is almost constant for a large part of the window. This is true for most of the lower-half and over the fore-upper quarter.

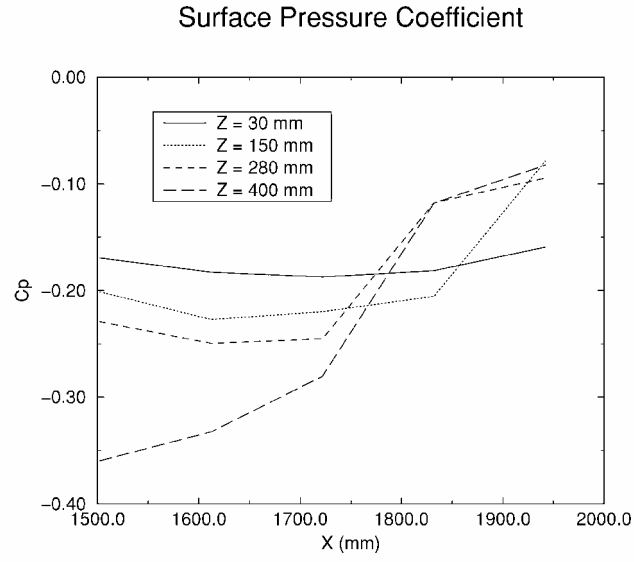

Fig. 18 Surface pressure coefficient, $M_\infty = 1.2$, angle of attack $\alpha = 1.4$ deg.

a)

b)

Fig. 19 Aerial photograph (courtesy of ELOP Electrooptics Industries, Inc.).

Figure 18 shows the surface pressure coefficient on the window for the flow at $M_\infty = 1.2$. The four lines correspond to the same heights as in Fig. 13. Once again, the pressure rise decreases as the height Z decreases. A zero pressure increase is experienced at the lower part of the window. As was mentioned before, the flow around the full-scale pylon and aircraft is expected to have a weaker shock, and the shock location is expected to be farther downstream of the location in the wind-tunnel experiment.

Verifying that scaling and viscous effects are indeed the sources for the differences between the numerical flow simulations results and the wind-tunnel experiment measurements is extremely difficult. It would be infeasible to conduct pressure measurements on a full-scale pod mounted on an aircraft in a supersonic flight. However, a clear photograph taken using the camera mounted on an aircraft flying at the critical condition would provide a proof as to the design concept. Figure 19a is a photograph taken from a flight height of 7,600 m and a speed of 1,200 km/h, which translates into an upstream Mach number of $M_\infty = 1.08$. The aerial distance from the camera to the center of the photograph is approximately 30,000 m. A clear photograph such is this could have been obtain only if no shocks were present around the window area. Figure 19b contains a closeup of the area marked by the square in Fig. 19a. Note the level of detail that is captured by the camera. Once again, such a clear photograph is possible only thanks to the shock free attached flow around the window.

Conclusions

The results from the numerical simulations presented in this paper show that a LOROP pod should be designed with flat planes, extending from the front part of the pod all of the way to the back, to accommodate the windows. This will allow sufficient longitudinal distance from the optical windows to the flat plane edges. Such a configuration is necessary to avoid flow separation and shocks in the window view area and, therefore, is essential to achieve a high level of aerooptical performance. The original geometry of the pod, containing the cavity to accommodate the window, caused massive flow separation in all flow conditions and an oblique shock, right across the window, in supersonic flows. The separation and shock occur due to the backward- and forward-facing steps that compose the upstream and downstream edges of the cavity. It is also shown that it is necessary to have a sharp cut discontinuity in the front part of the pod, where the flat plane starts, to keep the shock that appears on the flat plane forward of the window area.

The numerical simulations conducted about the complete aircraft configuration and the wind-tunnel test results show that a shock occurs on the pylon of the aircraft at transonic Mach numbers. At a Mach number of $M_\infty = 1.1$, the shock pattern predicted by numerical analysis slightly differs from the pattern found by wind-tunnel tests on a reduced-scale model, where the pylon shock occurs in the area of the optical window. The pylon shock causes a small pressure rise above the window, which causes a small density change and may cause flow separation. The effects of the pylon shocks can be significantly reduced by adding fences to the top edge of the optical window. Such fences would straighten the flow and, thus, would prevent the circumferential propagation of the pressure jump. Nevertheless, photographs taken by the camera at the critical Mach number of $M_\infty = 1.08$ show that the pylon shocks are not located around the window area and that the effects of the shocks do not hinder the performance of the camera.

Acknowledgments

The authors would like to thank D. Strash and M. Knapp of Analytical Methods, Inc., who ran the MGAERO full aircraft simulations discussed in this paper.

References

[1]Cook, N., "Royal Air Force Equips with Raptor," *Interavia*, Vol. 54, No. 629, March 1999, pp. 59–61.

[2]Gilbert, K. G., "Overview of Aero-Optics," *Aero-Optical Phenomena*, edited by K. G. Gilbert, and L. J. Otten, Progress in Astronautics and Aeronautics, Vol. 80, AIAA, New York, 1982, pp. 1–9.

[3]Sutton, G. W., "Aerooptical Foundation and Applications," *AIAA Journal*, Vol. 23, No. 10, 1985, pp. 1525–1537.

[4]Raveh, D. E., Levy, Y., and Karpel, M., "Structural Optimization Using Computational Aerodynamics," *AIAA Journal*, Vol. 38, No. 10, 2000, pp. 1974–1982.

[5]Levy, Y., "Numerical Simulation of Dynamically Deforming Aircraft Configurations Using Overset Grids," *Journal of Aircraft*, Vol. 38, No. 2, 2001, pp. 349–354.

[6]Raveh, D. E., Levy, Y., and Karpel, M., "Efficient Aeroelastic Analysis Using Computational Unsteady Aerodynamics," *Journal of Aircraft*, Vol. 38, No. 3, 2001, pp. 547–556.

[7]Baldwin, B. S., and Lomax, H., "Thin Layer Approximation and Algebraic Model for Separated Turbulent Flows," AIAA Paper 78-257, Jan. 1978.

[8]Degani, D., and Schiff, L. B., "Computation of Turbulent Supersonic Flows Around Pointed Bodies Having Crossflow Separation," *Journal of Computational Physics*, Vol. 66, No. 1, 1986, pp. 173–196.

[9]Degani, D., Schiff, L. B., and Levy, Y., "Numerical Prediction of Subsonic, Turbulent Flows over Bodies at Large Incidence," *AIAA Journal*, Vol. 29, No. 12, 1991, pp. 2054–2061.

[10]Degani, D., and Levy, Y., "Asymmetric Turbulent Vortical Flows over Slender Bodies," *AIAA Journal*, Vol. 30, No. 9, 1992, pp. 2267–2273.

[11]Cabral, B., and Leedom, L. C., "Imaging Vector Fields Using Line Integral Convolution," *Computer Graphics*, 1993, pp. 263–272.

[12]Forsell, L. K., and Cohen, S. D., "Using Line Integral Convolution for Flow Visualization: Curvilinear Grids, Variable-Speed Animation, and Unsteady Flows," *IEEE Transactions on Visualization and Computer Graphics*, Vol. 1, June 1995, pp. 133–141.

[13]Loser, T., Mewes, D., Levy, Y., and Hesselink, L., "Flow Visualization with Textures," *Chemie Ingenieur Technik*, Vol. 70, 1998, pp. 1382–1387.

[14]Loser, T., Mewes, D., Levy, Y., and Hesselink, L., "Flow Visualization with Textures," *Simulation, Image Processing, Optimization, and Control*, edited by F. Keil, W. Mackens, H. Voβ, and J. Werther, Scientific Computing in Chemical Engineering, Vol. 2, Springer-Verlag, Berlin, 1999, pp. 262–269.

[15]Heller, H. H., and Bliss, D., "The Physical Mechanism of Fluid-Induced Pressure Fluctuations in Cavities and Concepts for Their Suppression," *AIAA 2nd Aero-Acoustics Conference*, AIAA Paper 75-491, March 1975.

[16]Zhang, X., and Edwards, J. A., "Computational Analysis of Unsteady Supersonic Cavity Flows Driven by Thick Shear Layers," *Aeronautical Journal*, Vol. 92, No. 919, Nov. 1988, pp. 365–374.

[17]Suponitsky, V., "Numerical Investigation of Supersonic Flow Conditions over an Axisymmetric Cavity on a Blunt Cone," M.S. Thesis, Aerospace Engineering Dept., Technion—Israel Inst. of Technology, Haifa, Israel, Feb. 1999.

[18]Tidd, D. M., Strash, D. J., Epstein, B., Luntz, A., Nachshon, A., and Rubin, T., "Multigrid Euler Calculations Over Complete Aircraft," *Journal of Aircraft*, Vol. 29, No. 6, 1992, pp. 1080–1085.